

# Minimising Interference in Low-Pressure Supersonic Beam Sources

Jack Kelsall,<sup>1,\*</sup> Aleksandar Radić,<sup>1,\*</sup> David J. Ward,<sup>1</sup> and Andrew Jardine<sup>1</sup>

<sup>1</sup>*Cavendish Laboratory, Department of Physics, University of Cambridge, JJ Thomson Ave, Cambridge, UK*  
(Dated: October 30, 2024)

Free-jet atomic, cluster and molecular sources are typically used to produce beams of low-energy, neutral particles and find application in a wide array of technologies, from neutral atom microscopes to instruments for surface processing. However, understanding and maximising the intensity derived from such sources has proven challenging, partly because of gas interference effects attenuating the beam intensity. Here, we describe a semi-analytic method to estimate the resulting attenuation in low-pressure free-jet sources. We explicitly calculate two contributions to the interference, that arise from the interaction of the beam with (i) background gas and (ii) atoms backscattered from the skimmer. We demonstrate that the design of the skimmer has an insignificant impact for room temperature beams. Finally, we develop a number of design recommendations for the skimmer and vacuum chamber that optimise beam properties for spectroscopy and microscopy when using cryogenic-temperature atom or molecular beams.

## I. INTRODUCTION

A free-jet, or supersonic, source generates a thermal beam of neutral particles from a reservoir of gas and is used in a range of atomic, molecular and ion beam instruments. Free-jet sources have become the dominant mechanism for neutral species beam generation, with mostly empirical developments driving novel experimental techniques like atomic-scale lithography using metastable helium[1, 2], helium atom micro-diffraction[3–5], scanning helium microscopy[6–8] and ultrahigh resolution spectroscopy[9–12]. A thermal beam consists of particles with a low energy, given by  $E \sim k_B T$ , which, for example, gives beam energies  $\approx 60$  meV[3]. The probe particles are therefore unable to penetrate into any sample, leading to a non-destructive and exclusively surface-sensitive probe.

In a typical free-jet source, illustrated by Figure 1, gas behind a nozzle (typical diameter  $d \sim 10$   $\mu\text{m}$ ) is compressed to a high pressure (typically  $P_0 \sim 5 - 200$  bar)[13, 14]. The gas subsequently expands through the aperture at a high velocity, reaching supersonic speeds at the point where the cross sectional area is a minimum, often called the ‘throat’. As the gas expands into the vacuum, the mean free path increases until it reaches the ‘quitting surface’, a shell of finite thickness which is defined as the boundary volume where the mean free path exceeds the dimensions of the vacuum chamber, meaning that gas-gas interactions within the free-jet expansion become negligible. The region beyond the quitting surface is henceforth referred to as the ‘zone of silence’[13]. A complicated system of barrel shocks exist at the edges of the zone where the Mach number,  $M$ , drops below 1 and the expansion interacts with the background gas of the chamber[15, 16]. The properties of the shock depend on this background pressure, which is in turn determined by the pumping speed that manages the gas load. In order to develop

a beam, a skimmer is positioned in front of the nozzle to extract the centre of the expansion, thus defining the beam axis. The skimmer and its mount interact with the forward expansion, leading to backscattering and/or additional shock fronts which interfere with, and attenuate, the beam [17]. The diameter of the skimmer orifice is typically 100  $\mu\text{m} - 1$  mm, but microskimmers with smaller apertures exist and constitute an active area of research [18, 19].

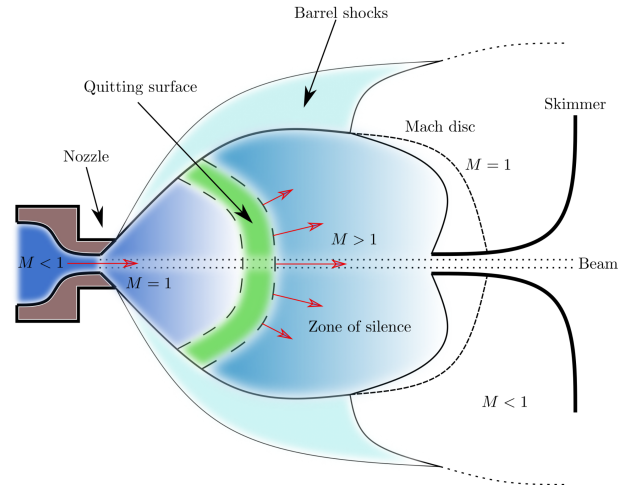


FIG. 1: A schematic of a free-jet expansion. The Mach disc and barrel shocks, where the expansion interacts with the background gas in the chamber, are relatively close to the skimmer, representing a typical geometry found in free-jet sources. The skimmer sits inside the zone of silence, within which there is free molecular flow, i.e. the beam particle mean free path is greater the dimensions of the chamber.

Interference is not solely determined by the geometry of the source. If the background pressure is very low (Fenn source), the expansion is in free molecular flow throughout most of the chamber[20, 21]. A non-negligible proportion of atoms scatter from the skimmer

\* These two authors contributed equally

towards the beam axis, leading to interference at low temperatures, when the momenta of all particles are small. By contrast, in the ‘Campargue’ regime where the background pressure is higher, there exist well-defined barrel shocks, and the Mach disc sits closer to the nozzle [22, 23]. As a result, the interference is more complicated and attenuation of the beam by ‘residual’ gas (which includes both the background gas and backscattered particles) is also relevant. Accounting for the background pressure is complicated by the fact that the shock fronts are relatively opaque to gas outside the zone of silence [14]. A practical solution to the issue of the additional interference is to lower the nozzle-skimmer distance,  $d_B$ , to reduce the length of the beam and hence the proportion scattered by the background gas. However, when  $d_B$  is reduced to the extent that it becomes comparable to the diameter of the skimmer orifice,  $d_S$ , the level of attenuation may rise as the supersonic expansion interacts with, and continues within, the skimmer itself. This finding can be understood qualitatively from the fact that the number density at the skimmer opening,  $n_S$ , is approximately proportional to  $1/d_B^2$ ; if the skimmer is placed closer than, or equal to, the nozzle than the quitting surface the gas is under-expanded and complex shock waves can form inside the tip of the skimmer. So-called ‘skimmer blocking’ may occur for very high flow rates [24].

There are few published models for source chamber interference and no true analytic ones. The simplest case of a Fenn source has been treated successfully using numerical simulations by Hedgeland et al., although these are not straightforward to run and interpret in practice [25]. While Verheijen et al. explored attenuation in a similar source, they relied on computationally expensive simulations and assumed a constant scattering cross section [26]. As a result, their theory contains free parameters which are estimated by fitting to the experimental data. A related work by Beijerinck et al. applies an analogous method to study the intensity of a Campargue source [23]. Interference within the skimmer itself can be modelled using Direct Simulation Monte Carlo (DSMC) methods [24, 27]. For very high number densities, a hybrid approach utilising continuum fluid mechanics is useful [28]. A consequence of the complexity of aforementioned semi-empirical approaches is that it is difficult to quantitatively compare different sources, hampering efforts to improve their design and thus their performance.

In the present work, we are concerned with sources in which (i) there is free molecular flow and (ii) the nozzle-skimmer distance is large enough that there is negligible interference within the skimmer. Such cases are amenable to an analytical treatment as the shocks formed are relatively simple. We determine the relationship between the mean number of interactions,  $\mu$ , and the measured signal, hence explaining the characteristic ‘turnover’ form of interference curves. We present both cryogenic and ambient temperature experimental data to support our calculations. We show that backscattering from the skimmer itself is the principal mode of interfer-

ence at low temperatures, whereas in room temperature sources, the interaction with the background gas dominates. We then present a series of design recommendations for skimmers and their mounts, principally for sources at cryogenic temperatures. Finally, by showing that modelling external interference can be reduced to a semi-analytical integral calculation containing no free parameters, we are able to address the issue of complexity in previous theories.

## II. THEORY

In our work, the molecular flow regime is assumed throughout the chamber, i.e. the quitting surface is taken to be very close to the nozzle. We also assume that the free-jet expansion is adiabatic, so we do not distinguish between the stagnation and quitting surface temperatures [13, 25].

### A. Soft-body scattering cross section

We first require a cross section,  $\sigma$ , for the interaction of the gas, that includes both background and backscattered particles, with the atoms in the beam. It has been found empirically that the scattering cross section between background and beam particles in long beam-axis systems is larger than the typical hard-body cross sections found in the literature because weak interactions are sufficient to cause deflections of the beam particles away from the axis, preventing transmission through the instrument [25]. A full derivation of the scattering cross section is presented in Appendix A, with the key features explained in the main text.

Consider a beam particle travelling along the  $z$ -axis with speed  $v$ . We define the speed of a background gas particle,  $u$ , with angle  $\theta$  relative to the negative  $z$ -direction. The situation is illustrated in the left-most panel of Figure 2. The centre of mass (CoM) and instantaneous rest frame (IRF) of the beam atom are also shown. In the latter, the speed of the residual atom is  $w = \sqrt{u^2 + v^2 + 2uv \cos \theta}$  and the angle  $\delta$  is given by  $\tan \delta = u \sin \theta / (v + u \cos \theta)$ .

We approximate the soft-body gas-phase interaction in terms of a van der Waals (VDW) potential with form  $V(r) = -C_6/r^6$ . The total deflecting impulse acting on a beam particle can then be evaluated, whereby the maximum allowable particle deflection is constrained by the acceptance angle,  $\Omega$ , defined by the nozzle and limiting aperture, which lies beyond the skimmer, such that:

$$\sigma = \left( \frac{15\pi C_6}{8mvv\Omega} \right)^{1/3} \int_{-\pi/2}^{\pi/2} (\cos^2 \varphi + \sin^2 \varphi \cos^2 \delta)^{1/6} d\varphi \quad (1)$$

A typical source geometry, as shown in Figure 1, has a large nozzle-limiting aperture distance compared to the skimmer’s diameter, making the acceptance angle  $\Omega \ll 1$ .

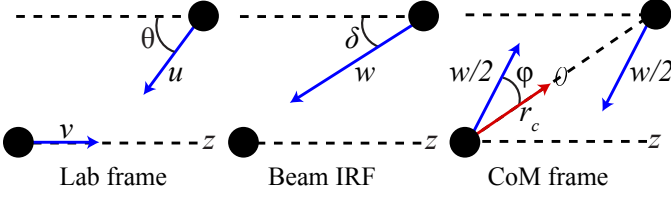


FIG. 2: Schematics of the three frames needed to derive the scattering cross section between the two atoms (black circles). The second and third diagrams correspond to the instantaneous rest frame (IRF) of the beam atom and the centre of mass (CoM) frame, respectively.

$v$  and  $w$  are the speeds of the beam and the background atoms in the IRF, respectively, and  $\delta$  is the angle between the beam and interfering particles, in the IRF of the beam.

### B. Interaction with backscattered particles

We begin by defining the basic geometry and coordinates of the source-skimmer assembly that will be referenced throughout, shown in Figure 3. The corresponding calculation scheme that will be used to evaluate the interference between backscattered or background gas and particles in the beam is shown in Figure 4. We employ

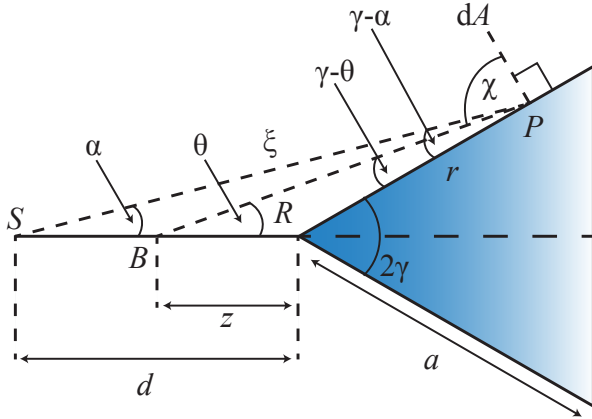


FIG. 3: A schematic diagram of a conical skimmer with an opening angle  $2\gamma$  at its tip. A source nozzle positioned at  $S$ ,  $B$  is an arbitrary point on the beam axis between source and skimmer tip, and  $P$  is an arbitrary point on the skimmer's surface.

a calculation scheme that splits the problem, which has cylindrical geometry, into conical subsections so that the method can be easily applied to arbitrary skimmer geometries. Following the stepwise labelled schematic diagram in Figure 4, the calculation scheme assumes an outgoing distribution of atomic flux from the nozzle towards the skimmer (1). Cosine-like scattering of the beam par-

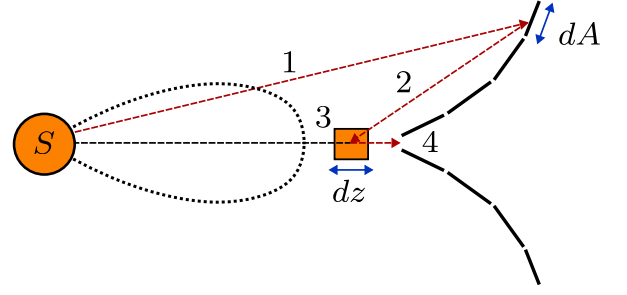


FIG. 4: A diagram showing the stages in the interference calculation. Atoms are emitted from  $S$ , according to a given distribution (dashed line), leading to a flux at the skimmer (1). Some of the particles are scattered towards the beam axis (2); they subsequently interfere with it according to a particular cross section (3) and slightly perturb the forward trajectories. The beam then passes through the skimmer (4) towards the detector.

ticles from the skimmer scatters a fraction back towards the beam axis (backscattered particles) (2). Using the previously derived scattering cross section, shown in 1, the interference between beam and backscattered atoms is calculated (3), perturbing atoms in the beam axis that eventually pass through the skimmer (4). We assume that all particles travel in straight lines between scattering events.

Comparing Figures 3 and 4, we must first express the distances  $\xi = SP$  and  $R = BP$  in an appropriate coordinate system. The distances correspond to calculations of the distributions of flux from the nozzle, and from the skimmer, steps (1) and (2) in the calculation scheme, respectively. Due to inherent symmetries in the generic source-skimmer geometries, we will use spherical polar coordinates  $(r, \theta, \varphi)$ . Taking  $P$  as a point on the skimmer, that lies a distance  $r$  from its tip, it has coordinates  $(x, y) = (d + r \cos \gamma, r \sin \gamma)$ . The point  $B$  lies on the beam, a distance  $z$  from the skimmer tip.  $dA = r \sin \gamma dr d\varphi$  is the area element of the skimmer at  $P$ . The distances  $\xi$  and  $R$  are given by

$$\xi^2 = d^2 + r^2 + 2dr \cos \gamma, \quad (2)$$

$$R^2 = z^2 + r^2 + 2zr \cos \gamma. \quad (3)$$

From Figure 3,  $\cos \alpha = (r \cos \gamma + d)/\xi$  and  $\cos \theta = (r \cos \gamma + z)/R$ . To simplify the following calculations, an assumption must be made regarding the shape of the forwards expansion in Figure 4. Beijerinck and Verster's widely used approximation is:

$$\frac{df}{d\Omega} = \frac{p+1}{2\pi} \cos^p \alpha, \quad (4)$$

where  $d\Omega$  is an element of solid angle and  $df$  is the probability of scattering into  $d\Omega$  at  $\alpha$ [29]. A peaking factor,

$p$ , of 4 (relative to a uniform hemispherical distribution for which  $p = 1$ ) is expected for a monatomic gas.

The flux of atoms at  $P$  can be calculated from (4) and the total flow of particles through the nozzle,  $\dot{N}$ . Resolving perpendicular to the skimmer's surface to obtain the component of the flux,  $F$ , incident on  $dA$ ,

$$F = \frac{\dot{N}}{\xi^2} \frac{df}{d\Omega} \sin(\gamma - \alpha) = \frac{(p+1)Qd \sin \gamma \cos^p \alpha}{2\pi k_B T_0 \xi^3}, \quad (5)$$

where we have used  $\sin(\gamma - \alpha) = d \sin \gamma / \xi$  and  $Q = p_0 \dot{V} = \dot{N} k_B T_0$  for stagnation pressure  $p_0$ , nozzle temperature  $T_0$  and volumetric flow rate  $\dot{V}$ . The nozzle throughput,  $Q$ , is a measurable quantity with units  $\text{mbar L s}^{-1}$ .

To evaluate the flux that is backscattered towards the beam-axis, step (2) in the calculation scheme, we now consider scattering from the skimmer surface element  $dA$  using  $F$ , such that eventually the flux of interfering particles reaching point  $B$  can be found. There is a cosine distribution for diffuse scattering from rough or 'unclean' surfaces covered by adsorbates [30–32], meaning that the probability per solid angle of a particle being scattered to an angle  $\chi$  is

$$\frac{df}{d\Omega} = \frac{1}{\pi} \cos \chi. \quad (6)$$

Now consider scattering towards the beam axis. The rate of particles striking the element  $dA$  is  $F dA$ . Hence, the rate of scattering towards  $B$  is  $F dA df$ . Also consider a small area  $dS = R^2 d\Omega$  at  $B$ , normal to the  $\chi$  direction, at which the flux is  $dF_z = F dA df / R^2 d\Omega$ . We assume that the attenuation of the backscattered flux by the forwards expansion in the intervening region is negligible. Using  $\chi = \pi/2 - (\gamma - \theta)$ ,  $\sin(\gamma - \theta) = z \sin \gamma / R$  and the expression for  $dA$ ,

$$dF_z = \frac{F \sin^2 \gamma}{\pi R^3} z r dr d\varphi. \quad (7)$$

Only a finite fraction of the particles scatter elastically from the skimmer. In the the remaining subset, there is a spread of energy transfers, including a small number of particles that attain the skimmer temperature,  $T_S$ . The energy accommodation coefficient,  $\lambda$ , is a measure of the efficiency of energy exchange between a surface and colliding gas-phase molecules, averaged over all interactions [33]. In order to account for the non-zero value of  $\lambda$  in our calculations in a simple manner, we assume that a fraction,  $\lambda$ , of all particles incident on the skimmer and chamber leave with a temperature  $T_S$ , while the remaining portion retain their original temperature  $T_0$ . In the calculations that follow, we use  $\lambda = 0.15$ , given that the accommodation coefficients for He on adsorbate-covered nickel and stainless steel (of which the skimmer and chamber are composed) are 0.156 and  $\sim 0.15$ , respectively [34].

The distribution of speeds of the accommodated particles can be taken into account using a Maxwell-Boltzmann distribution, so the probability of leaving with a speed  $u \rightarrow u + du$  is

$$df_u = g du = 4\pi u^2 \left( \frac{m}{2\pi k_B T_S} \right)^{3/2} e^{-mu^2/2k_B T_S} du. \quad (8)$$

The distribution of beam speeds does not resemble (8). However, for high Mach numbers, the distribution approaches a delta function. In other words, it is sufficient to assume that  $v = v_0$ , where

$$v_0 = \sqrt{\frac{2\kappa}{\kappa-1} \frac{k_B T_0}{m}}. \quad (9)$$

The above can be derived from an analysis of the flow through a de Laval nozzle [13].  $\kappa$  is the adiabatic ratio with a value of 5/3 for a monatomic gas.

The mean number of interactions can be computed by working in the beam IRF at  $B$  and considering particles incident on the element. The number density,  $dn$ , associated with  $dF_z$  is invariant, so the flux in the IRF is

$$dF'_z = dn w = \frac{w}{u} dF_z. \quad (10)$$

The number of interactions for an atom in the beam in the element of length  $dz$  during  $dt$  is

$$d\mu_S = dF'_z \sigma dt df_u, \quad (11)$$

where  $\sigma$  is the previously derived scattering cross section. Note that (11) is also invariant.  $dt = dz/v_0$  enables a change of variables to  $z$ . The final expression for  $d\mu_S$ , expressed as a sum of the elastically scattered and thermally accommodated terms, is

$$d\mu_S = \frac{(p+1)Qd \sin^3 \gamma}{2\pi^2 k_B T_0 v_0} \frac{z r w \sigma \cos^p \alpha}{u \xi^3 R^3} \times [(1-\lambda)\delta(u-v_0) + \lambda g] dr d\varphi dz. \quad (12)$$

Taking (12) and defining a flow-independent attenuation coefficient due to backscattering,  $\eta_S$ , by  $\mu_S \equiv \eta_S Q$ , allows us to write the exact integral form of  $\eta_S$  as

$$\eta_S = \frac{(p+1)d \sin^3 \gamma}{\pi k_B T_0 v_0} \int_0^\infty \int_{r_-}^{r_+} \int_{d-d_B}^d \frac{z r w \sigma \cos^p \alpha}{u \xi^3 R^3} \times [(1-\lambda)\delta(u-v_0) + \lambda g] dz dr du. \quad (13)$$

Following the calculation scheme we have arrived at an exact expression for the beam attenuation due to backscattered particles,  $\eta_S$ , that is applicable to arbitrary, realistic skimmer geometries, but cannot be solved

analytically (13). Using Figure 3 for reference, the problem can be approximated by assuming that the half angle at the skimmer tip is small,  $\gamma \ll 1$ , taking the source nozzle aperture, located at  $S$ , to have a negligible radius compared to the source-skimmer tip distance,  $d_B$ , and taking all angles to be small. We can now integrate (13) and find the following approximate analytic solution

$$\eta_S \approx \underbrace{\frac{(p+1)\gamma^3}{16d_B k_B T_0}}_{\text{a) Free-jet expansion}} \underbrace{\left(\frac{15\pi C_6}{mv_0^4 \Omega}\right)^{1/3}}_{\text{b) Gas-phase scattering}} \underbrace{\left[1 - \frac{1}{(1+a/d_B)^4}\right]}_{\text{c) Skimmer geometry}} \underbrace{I_u}_{\text{d) Inelastic effects}}. \quad (14)$$

The equation can be interpreted as being composed of four components. (a), describes the shape of the free-jet expansion from the source aperture, (b), describes the interaction between backscattered and beam particles, and, (c), defines the geometry of the source, skimmer and skimmer plate. The final term,  $I_u$ , accounts for inelastic scattering events between beam particles and the skimmer or skimmer plate, and is primarily controlled by the fraction of scattering events after which the scattered particle has speed corresponding to the temperature of the scattering surface rather than its initial speed. The complete form of  $I_u$  is

$$I_u = \int_0^\infty \frac{(u+v_0)^{2/3}}{u} [(1-\lambda)\delta(u-v_0) + \lambda g] du. \quad (15)$$

For no energy accommodation of the scattered particles, such that  $\lambda = 0$ ,  $I_u = (4/v_0)^{1/3}$ . A crucial finding from (14) is that  $\eta_S \propto \gamma^3$ , so the interference increases very sharply as the angle is made larger. However, the skimmer backing plate, which is increasingly obscured as  $\gamma$  rises, may need to be taken into account, depending on the extent of the Mach disc.

A comparison between the numerical solution to the exact, (13), and the approximate analytic, (14), expressions for  $\eta_S$  is evaluated graphically in Figure C1, Appendix C and shows good agreement between the solutions. In Appendix B we show how a generic continuous profile function to describe a skimmer can be implemented into (14) and an approximate analytic form is found. In Appendix C the continuous profile function is applied for the case of a parabolic skimmer profile as an example, with results plotted in Figures C4.

### C. Interaction with background particles

To find an expression for the beam particles' interaction with background gas, we consider the lab frame in Figure 2, in which the flux of background atoms,  $dF$ , is

$$dF = n u d f_u d f_\theta, \quad (16)$$

where  $d f_u$ , as in (8), is the fraction of background particles with speed  $u \rightarrow u + du$  while  $d f_\theta$  is the probability that a particle moves towards the beam at an angle  $\theta \rightarrow \theta + d\theta$ . Assuming the background gas is completely randomised,  $d f_\theta$  is proportional to the solid angle between  $\theta$  and  $\theta + d\theta$ . By normalisation,  $d f_\theta$  becomes

$$d f_\theta = \frac{1}{2} \sin \theta d\theta, \quad (17)$$

where  $n$  is the number density of the background gas. In the sources we consider,  $n$  is approximately constant in the source chamber and is given by

$$n = p_C / k_B T_C, \quad (18)$$

for chamber pressure,  $p_C = Q/S$ , where pumping speed is  $S$ , and chamber temperature  $T_C$ . Equation 18 is most accurate in Fenn-type sources, where the weak shock structure is unable to prevent most of the external gas from passing into the zone of silence. In Campargue sources, the stronger shocks mean that  $n$  is likely to be smaller.

Substituting (17) and (18) into (16) we can express the flux of background atoms in the lab frame as

$$dF = \frac{uQ \sin \theta}{2Sk_B T_C} d f_u d\theta. \quad (19)$$

We now transform (19) from the lab frame into the beam IRF using (10), to arrive at

$$dF' = \frac{wQ \sin \theta}{2Sk_B T_C} d f_u d\theta. \quad (20)$$

Following from (11), the mean number of scattering events between beam and background particles is  $d\mu_B = dF' \sigma dt$ , so (20) becomes

$$d\mu_B = \frac{wQg\sigma \sin \theta}{2Sk_B T_C v_0} d\theta du dz, \quad (21)$$

which is analogous to (12) for the case of interaction between an atom in the beam and backscattered particles. By definition, the mean number of scattering events relates to the beam attenuation coefficient by  $\mu_B \equiv \eta_B Q$ . Applying this relation to (21) and integrating gives

$$\eta_B = \frac{d_B}{2Sk_B T_C v_0} \int_0^\infty \int_0^\pi w \sigma \sin \theta g d\theta du. \quad (22)$$

The integral for  $\eta_B$  cannot be evaluated analytically. However, for a nozzle temperature that is much less than the chamber temperature,  $T_0 \ll T_C$ , the mean speed of interfering particles is much greater than the speed of those in the beam, meaning that  $u \gg v_0$ . As a result the relative speed of background particles, in the beam IRF, is approximately equal to their speed in the lab frame

such that  $w \approx u$ , allowing us to arrive at the following approximate analytical solution,

$$\eta_B \approx \overbrace{\frac{5\Gamma(5/6)d_B}{12S}}^{\text{a) Effective path length}} \underbrace{\left[ \frac{30C_6}{\sqrt{\pi}\Omega(mk_BT_C)^2 v_0^4} \right]}_{\text{b) Scattering cross section}}^{1/3} \overbrace{I_\theta}^{\text{c) Inelastic effects}}, \quad (23)$$

where  $\Gamma$  is the gamma function. The approximate solution can be broadly described as consisting of three components. Part a) describes the effective path length of a beam particle through the interfering background gas that is primarily a function of nozzle-skimmer distance,  $d_B$ , and pumping speed,  $S$ , b) introduces the soft-body VDW potential for gas-phase scattering and describes the overall scattering cross section between beam and background particles, and c) encapsulates inelastic scattering effects within a function  $I_\theta$ , a numerical constant calculated from

$$I_\theta = \int_0^\pi \int_{-\pi/2}^{\pi/2} (\cos^2 \varphi + \sin^2 \varphi \cos^2 \theta)^{1/6} \sin \theta d\varphi d\theta \approx 5.72. \quad (24)$$

For completeness we plot the exact and approximate expressions for  $\eta_B$  in Figure D1, Appendix D using  $T_C = 293$  K and  $S = 2500$  Ls<sup>-1</sup>, showing excellent agreement between the solutions. However, a different pumping speed simply leads to a re-scaling of all values of the coefficient, because  $\eta_B \propto 1/S$ .

#### D. Relationship between attenuation coefficient and measurable signal

The mean total number of interactions that deflect a particle from the beam is simply a sum of the terms due to direct backscattering and background gas, i.e  $\mu = \mu_S + \mu_B$ . Each is proportional to  $Q$ , so the total attenuation coefficient is  $\eta = \eta_S + \eta_B$ .

To find a relationship between  $\mu$  and the signal,  $W$ , Poisson statistics can be applied, given that the disruptive interactions are independent events in the limit of small-angle scattering. Thus, the probability that a particle suffers  $n$  collisions is  $P(n) = \mu^n e^{-\mu}/n!$ . The probability of zero events, which must be the same as the detected fraction of the beam, is  $P(0) = e^{-\mu}$ . The signal is proportional to the nozzle throughput in the absence of interference, so

$$W \propto Qe^{-\eta Q}, \quad (25)$$

which implies that the signal is maximal for a throughput of  $Q_M = 1/\eta$ . Experimental data fitted to (25) is shown in top panels of Figure 5. The fact that the signal can be

modelled by  $Qe^{-\eta Q}$  is significant, irrespective of our theory to calculate  $\eta$ , because it means that source chamber interference can be quantified by a single parameter.

However, many signal-throughput curves do not resemble the form given by (25). A plateau, rather than a turnover, in signal is commonly observed [19]. The vast majority of such deviations can be attributed to the use of high-pressure (i.e. non-Fenn type) sources, in which problematic shock waves at the skimmer entrance develop. Studies have shown that cooling the skimmer to suppress such shock waves may completely eliminate the interference [24]. Once this so-called skimmer ‘blocking’ is accounted for, (25) is still applicable.

#### E. Evaluating the scattering coefficient of a chamber

In the calculations that follow, we consider an axisymmetric vacuum chamber described in profile by coordinates  $\mathbf{x}$  and  $\mathbf{y}$ , such that an individual element is represented by  $(x_i, y_i) \rightarrow (x_{i+1}, y_{i+1})$ . Each element is described by an angle  $\gamma_i$ , an effective nozzle-tip distance  $d_i$  and limits of integration such that  $r \in [r_i^-, r_i^+]$  where

$$\gamma_i = \tan^{-1} \left( \frac{y_{i+1} - y_i}{x_{i+1} - x_i} \right), \quad (26)$$

$$d_i = \frac{y_{i+1}x_i - y_ix_{i+1}}{y_{i+1} - y_i}, \quad (27)$$

$$r_i^- = y_i \sqrt{1 + \left( \frac{x_{i+1} - x_i}{y_{i+1} - y_i} \right)^2}, \quad (28)$$

$$r_i^+ = y_{i+1} \sqrt{1 + \left( \frac{x_{i+1} - x_i}{y_{i+1} - y_i} \right)^2}. \quad (29)$$

Geometrical shadowing may also occur in two ways. First, shadows cast by particular elements prevent others from being illuminated by the forward expansion. The occluded elements therefore cannot contribute to the attenuation. Second, particles scattered towards the beam axis may be blocked by intervening elements. As a result, the effective length of the beam viewed from certain scattering points may be reduced, which can be accounted for by making the beam length in (13) a function,  $d_B(r)$ .

The Mach disc, beyond which the flow ceases to be supersonic, must also be considered. Approaching the disc,  $M \rightarrow 1$  and the number density rises rapidly, meaning that molecules reaching the boundary interact with it and have their velocities randomised. As a result, the disc is partially opaque to the supersonic expansion and so any elements of the source chamber lying behind it contribute less to  $\eta_S$  [13]. The position of the disc is given by

$$x_M = 0.67D\sqrt{\frac{p_0}{p_c}}. \quad (30)$$

Here,  $D$  is the nozzle diameter. The dimensionless coefficient of (30) is empirical, although the result has a sound theoretical basis [35]. There is experimental evidence to suggest that excluding parts of the source beyond the Mach disc is valid [36]. We therefore include the disc in our calculations, and neglect the contribution of any elements beyond it to  $\eta_S$ .

Once a routine to account for shadowing and the Mach disc is implemented, one can calculate  $\eta_S$  for each element. The total value is the sum over all of the individual coefficients. An alternative approach, in which the skimmer is described by a continuous profile function  $f = f(x)$ , is given in Appendix B.

### F. Scaling relationships

Both  $\eta_S$  and  $\eta_B$  rise as the nozzle temperature (and hence beam momentum) falls. For  $\lambda = 0$ ,  $\eta_S$  obeys

$$\eta_S \propto 1/T_0^{11/6}. \quad (31)$$

The proportionality relationship for  $\eta_B$  is more complicated as  $T_0$  appears in the integrand of (22). However, for chamber temperature  $T_C \gg T_0$  equation (23) gives,

$$\eta_B \propto 1/T_0^{2/3}. \quad (32)$$

$\eta_B$  therefore depends more weakly on nozzle temperature than  $\eta_S$ . The difference arises from the fact that scattering by the background gas molecules is determined by  $T_C$ , whereas  $T_0$  dictates the speed of the majority of the particles that contribute to  $\eta_S$ . Therefore, because  $\eta_B$  decreases less than  $\eta_S$  as the nozzle temperature  $T_0$  rises, (32) and (31) together imply that there is a transition from ‘skimmer interference’ to background-dominated attenuation. We discuss experimental evidence for the phenomenon in Section III. The existence of a transition implies that there is limited benefit to carefully optimising the design of skimmer geometries used with ambient temperature sources.

The dependence of each attenuation coefficient on the nozzle-skimmer distance,  $d_B$ , can also be discussed. The background coefficient,  $\eta_B$ , obeys

$$\eta_B \propto d_B, \quad (33)$$

given that it represents Beer’s law interference. However, the backscattering attenuation coefficient,  $\eta_S$ , drops off rapidly as  $d_B$  increases. For large  $d_B$ ,

$$\eta_S \propto 1/d_B^2, \quad (34)$$

which follows from the inverse-square law for the flux of the supersonic expansion arriving at the skimmer. Furthermore, because the two coefficients vary oppositely with  $d_B$ , the theory predicts a distance at which the interference is minimal (i.e.  $\partial\eta/\partial d_B = 0$ ). Such a maximum in signal is observed experimentally [13, 36]. Even so, a calculation of the optimum position using the theory here is unlikely to be accurate for all sources. For example, interference within the skimmer itself, which is best modelled using DSMC methods due to the complex shock structures involved, may contribute for high throughputs and small nozzle-skimmer distances [24].

## III. EXPERIMENTAL DATA

Here we present three sets of interference curves, corresponding to source chambers operating in different regimes, to support our theory. Each is fitted to  $W \propto Qe^{-\eta Q}$ , which is applicable in all cases. The attenuation coefficients,  $\eta$ , are modelled using Equations (13) and (22). The throughput,  $Q$ , is calculated from the stagnation pressure,  $p_0$ , via the empirical relationship

$$Q = C\sqrt{\frac{T_C}{T_0}}p_0D^2 \quad (35)$$

which has been verified for the relevant sources [36, 37]. For  $^4\text{He}$ ,  $C = 450 \text{ ms}^{-1}$  [13]. A theoretical expression for  $Q$ , derived by considering the fluid mechanics of a converging-diverging de Laval nozzle, reveals that  $C \propto 1/\sqrt{m}$  [13]. Hence,  $C$  for  $^3\text{He}$  is  $\sqrt{4/3}$  times the  $^4\text{He}$  value.

### A. A cryogenic source - backscattering-dominated attenuation

We first consider a cryogenically cooled source between 22 – 37 K with a conical skimmer geometry, situated in the Cambridge  $^3\text{He}$  spin-echo spectrometer and henceforth referred to as ‘Source 1’[38], in which the nozzle-skimmer distance is 6.2 mm and the pumping speed is  $S \approx 3000 \text{ L s}^{-1}$ . The source contains a  $D = 10 \text{ }\mu\text{m}$  nozzle and a limiting aperture along the beam axis with an angular radius of  $\Omega = 1.366 \times 10^{-3} \text{ rad}$ . The signal reflected from a sample at specular orientation in the scattering chamber was recorded using a custom He atom detector [39]. A schematic of the source-skimmer geometry is shown in Figure E1, with a selection of the signal-flow curves and both experimental and theoretical values of  $\eta$  shown in the left-hand panels of Figure 5. No free parameters were used in the fitting of Equations (13) to the experimental data. For simplicity, the background attenuation has been neglected, given that the low temperatures and small nozzle-beam distance ensure that  $\eta_B$  is substantially less than  $\eta_S$ . Overall, there

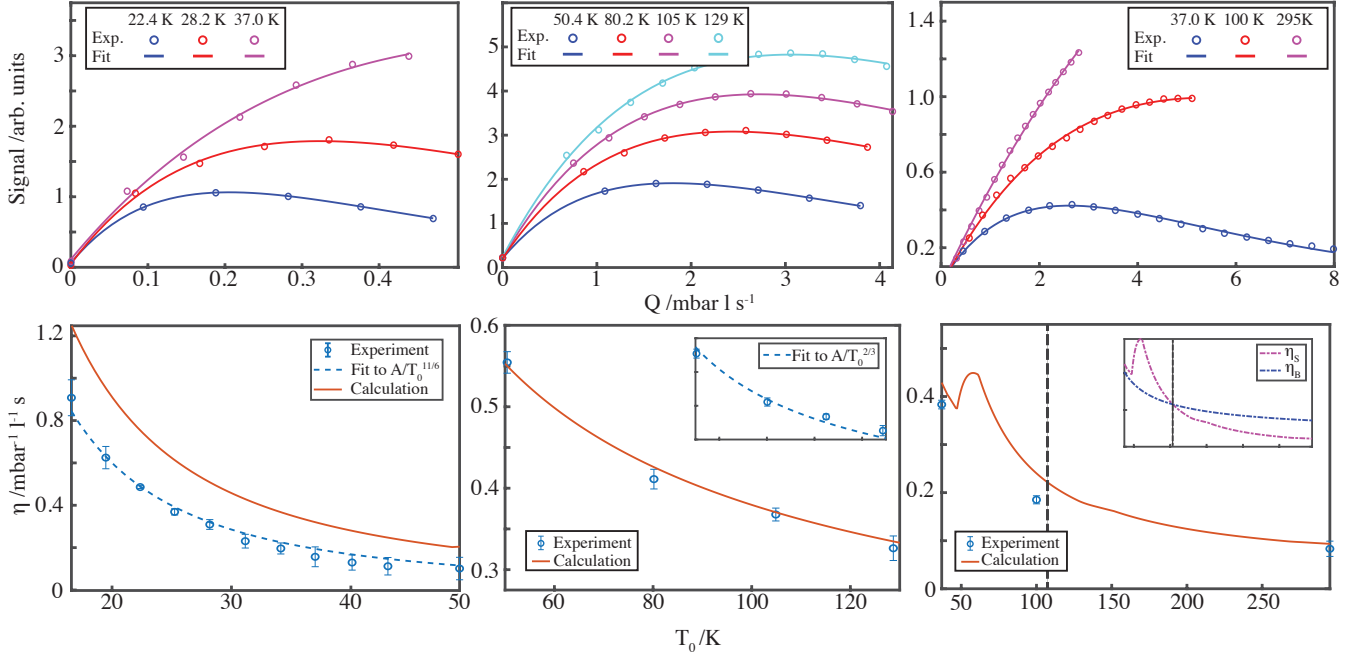


FIG. 5: Top - a selection of signal-flow curves for Sources 1-3 (left to right) and a fit  $W \propto Qe^{-\eta Q}$  to each of them. Signal units are arbitrary and curves have been re-scaled for clarity. Schematic cross sections of the source-skimmer geometries for each instrument can be found in Figure E1. Bottom - measured and calculated values of the attenuation coefficient,  $\eta$ , for Sources 1-3 from left to right. A change in beam attenuation regime, from backscattered to background, is denoted by a vertical dashed line in the bottom-right panel. No free parameters were used to obtain the calculated lines.

is reasonable agreement, and the approximate relationship  $\eta_S \propto 1/T_0^{11/6}$  (dashed line) fits the experimental data well. The results constitute strong evidence that at low temperatures, backscattering is the dominant interference mechanism.

### B. A high-pressure source - background-dominated attenuation

We also consider ‘Source 2’, a <sup>4</sup>He source found on the Cambridge helium diffractometer, ‘MiniScat’ [36]. Although similar stagnation temperatures were used to obtain the previous and present datasets, the two sources operate in very different regimes; the pumping speed on Source 2 (estimated at 1200 L s<sup>-1</sup>) is considerably lower and the nozzle-skimmer distance ( $d_B = 12$  mm) is also larger. As a result, the attenuation of the beam is dominated by the diffuse background gas. The source contains a  $D = 10$   $\mu$ m nozzle and the limiting aperture along the beam axis, with an angular radius of  $\Omega = 1.93 \times 10^{-3}$  rad, lies just before the scattering chamber. The geometry of the source is otherwise identical to that of Source 1, as seen in Figure E1, Panel (a). A selection of signal-flow curves, measured using a Hiden mass spectrometer, are displayed in top-center panel of Figure 5. The extracted values of  $\eta$  are plotted in the bottom-center panel of Fig-

ure 5, alongside the theoretical result from (22). For simplicity, the attenuation due to the skimmer and mount has been neglected, as  $\eta_S \ll \eta_B$ . There is excellent agreement, and the approximate relationship  $\eta_B \propto 1/T_0^{2/3}$  (dashed line) fits the experimental data well.

### C. Evidence for a transition in the interference mechanism

Finally, we consider ‘Source 3’, for which theoretical and experimental data from Hedgeland et al. [25] have been used in this work. The data constitute a severe test of the theory, given that the nozzle temperature varies over an order of magnitude, from 27 – 295 K. Source 3 operates uses <sup>4</sup>He and its source-skimmer geometry is shown in Figure E1, Panel (b). The nozzle-skimmer distance is relatively large (15 mm) as a diffusion pump capable of  $S = 4500$  L s<sup>-1</sup> is installed on the chamber, making background attenuation less problematic. The nozzle diameter is 18.5  $\mu$ m and the limiting aperture was found to produce a beam with an angular radius of  $\Omega = 2.74 \times 10^{-3}$  rad. In the right-most panels of Figure 5, the experimental and theoretical values of  $\eta$  are plotted as a function of the stagnation temperature,  $T_0$ . Both contributions to the calculated coefficient, corresponding to (13) and (22), are graphed separately in the inset. There



is good agreement, and a transition from backscattering-to background-dominated interference is clearly visible, marked by a dashed black line in the bottom-right panel of Figure 5, supporting the relations determined in Subsection II F.

A notable feature of the bottom-right panel in Figure 5 is the small dip and rise in the coefficient as the temperature increases near 37 K, which can be attributed to  $\eta_S$  rising as the Mach disc moves backwards (because  $x_M \propto T_0^{1/4}$ ). As a result, more elements of the source chamber become exposed to the expanding gas and thus contribute to the attenuation by backscattering. In reality, the feature is not observed because the Mach disc is poorly modelled by a sharp boundary where it interacts with the skimmer and chamber [23]. A more accurate, diffuse model for the disc would lead to a smoothing out of  $\eta$  at low temperatures.

#### IV. SOURCE CHAMBER DESIGN OPTIMISATION

One may use the attenuation coefficient,  $\eta$ , to minimise interference in, and thus optimise, the design of skimmers in Fenn-type sources. Here, we discuss some general principles based on our theory, alongside a discussion of the optimal skimmer design. We also qualitatively discuss other types of interference which cannot necessarily be ignored. It should be noted that a small drop in  $\eta$  corresponds to a substantial increase in signal for the same throughput,  $Q$ , as the attenuation depends exponentially on the coefficient. Quantitatively, a reduction in its value of  $\Delta\eta$  leads to the signal being  $e^{\Delta\eta Q}$  times as large.

##### A. Principle 1: the skimmer design in room-temperature sources isn't critical

In typical Fenn-type sources operating at room temperature, the design of the skimmer and chamber should have a negligible impact on the beam intensity, and any attenuation should principally be due to the interaction with the background gas. Conversely, in cryogenic sources, there is diminishing benefit to installing more effective pumps to reduce the chamber pressure as backscattering is more important. Consequently, there should be little difference between a simple conical skimmer, which could be cheaply and rapidly 3D-printed[40], and a flared, polished design which necessitates advanced tooling.

For room temperature beams, our theory predicts that (i) reducing the beam length  $d_B$  and (ii) increasing the pumping speed  $S$  have the greatest positive impact on the transmitted intensity. Although increasing  $S$  is generally beneficial, reducing the nozzle-skimmer distance too much may lead to internal interference and/or the formation of shock waves. However, cooling the skimmer to  $\sim 30$  K has been shown to suppress such shock

waves, with the precise temperature dependent on the gas utilised [24]. Further discussion of shocks and their suppression is beyond the scope of the present work.

Henceforth, the discussion will only apply to cryogenic sources, in which attenuation due to backscattering from the skimmer and mount is not negligible.

##### B. Principle 2: avoid perpendicular surfaces

The benefits of a curved skimmer, with a shallow angle to the beam axis along most of its length, are well-understood on the basis of cosine scattering[8]. However, many skimmer mounts are designed with plane surfaces perpendicular to the beam and/or expansion. Given that such components are not necessarily shielded by the Mach disc, it is important to consider more than just the skimmer when minimising interference.

To illustrate the principle, we consider a  $^4\text{He}$  source, depicted in Figure 6, consisting of a conical skimmer and a back plate. We assume that the pumping speed is large, such that the Mach disc lies behind the arrangement. In the calculations of  $\eta_S$ , the results of which are stated in the image, we take  $\Omega = 1.366 \text{ rad}^{-1}$  and  $T_0 = 37 \text{ K}$ . Scattering from the skimmer accounts for 64 % of the attenuation coefficient, meaning that the mount contributes the remaining 36 % despite it being much smaller and positioned further from the beam. The proportions are almost temperature independent. We then consider the same source chamber with a new mount, such that its face is at  $45^\circ$  to the beam axis, which is also shown in Figure 6. The mount is projected outwards to avoid interfering with the brim of the skimmer. The total contribution of the mount to the attenuation coefficient drops to 20 %, and  $\eta_S$  is significantly less.

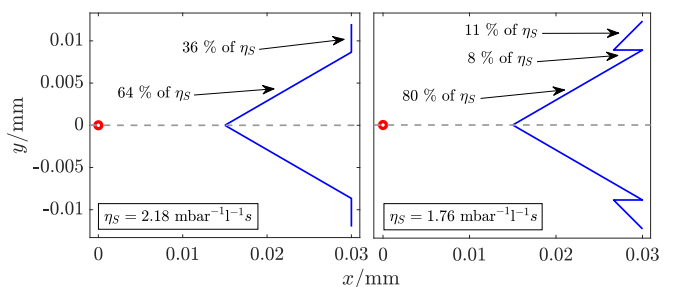


FIG. 6: A sketch of the two sources considered in the calculations to determine the effect of the skimmer mount. Left - a conical skimmer with a ‘conventional’ mount, consisting of a flat ring around the base. Right - the hypothetical source with the front of the mount at  $45^\circ$  to the beam axis.

### C. Principle 3: skimmer apertures are problematic

Further to the discussion Subsection IV B, our theory suggests that inserting an aperture or glass microskimmer into the end of a standard skimmer is likely to result in significantly more beam attenuation. An element near the beam axis naturally leads to more interference, by the inverse-square law for flux involved, and perpendicular faces - such as those of an aperture - are particularly problematic. A number of designs, including microskimmers, have been tested in the context of intensity and brightness measurements by Palau et al. [41]. They also consider a so-called Kurt skimmer with an indented tip specifically designed to increase attenuation so that it can be studied. Although their measurements relate to relatively warm sources, where temperatures investigated were ambient and  $\approx 125$  K, they still conclude that skimmer interference due to the Kurt skimmer's tip geometry is significant.

Here we illustrate the point by comparing a conical skimmer to the Kurt design, with the latter depicted in Figure 7 alongside its relevant dimensions. The two skimmers are identical aside from the tip. The length of each is taken to be  $l = 15$  mm, we assume a nozzle-skimmer distance of  $d_B = 15$  mm and neglect the skimmer mount for simplicity. We consider a  $^4\text{He}$  source at  $T_0 = 37$  K and take  $\Omega = 1.366 \times 10^{-3}$  rad. For such low nozzle temperatures, the results are striking;  $\eta_S = 12.5 \text{ mbar L s}^{-1}$  for the Kurt skimmer while  $\eta_S = 0.391 \text{ mbar L s}^{-1}$  for the equivalent conical skimmer. In other words, the perpendicular face and indent of the Kurt skimmer result in overwhelming interference, and contribute 50 % and 46 % to the total value of  $\eta_S$ , respectively. The calculations support the widely accepted principle that skimmer orifices must be sharp and thin. Although the work by Palau et al. is qualitative evidence in support of our results, deviations from our theory are expected if the structure of the skimmer tip leads to blocking and the formation of shock waves.

Further calculations reveal that  $\eta_S$  and  $\eta_B$  are comparable at room temperatures. Therefore, although Kurt skimmers are impractical at cryogenic temperatures due to the excessive interference they cause, they are still useable in ambient temperature sources. By extension, glass microskimmers - which also have large values of  $\eta_S$ , although not to the same extent as Kurt skimmers - are expected to be acceptable in room-temperature sources but problematic otherwise.

### D. Principle 4: a narrow skimmer is not necessarily superior

There are two reason why a narrow skimmer is not necessarily superior to one with a broader base. The first has been alluded to in Subsection IV A; internal interference may be problematic in narrow skimmers, especially when the gas is underexpanded and the number density is high

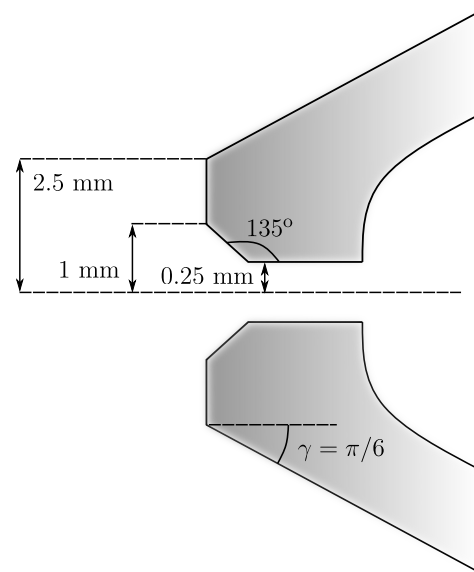


FIG. 7: A schematic of the tip of a Kurt skimmer, with the relevant dimensions indicated. The rest of the skimmer is conical, with a length of 15 mm and no mounting plate. We take the nozzle-skimmer distance to be  $d_B = 15$  mm in the calculations.

at the orifice [24, 27]. A minimum opening angle at the skimmer aperture may therefore be needed to prevent ‘blocking’. The second relates to skimmer mount; as the skimmer is made narrower, more of the chamber behind it is exposed to the forwards expansion. As discussed in Subsection IV B, the resulting contribution to the attenuation may be significant and overcome the benefit of sharpening the skimmer.

We consider a simple system to illustrate the point, depicted in the inset of Figure 8, consisting of a conical skimmer and back plate. However, the conclusions generalise to curved skimmers and more complicated geometries. We vary the angle,  $\gamma$ , at the skimmer opening and plot the results in Figure 8. We consider a similar system, Source 2, which uses  $^4\text{He}$  at  $T_0 = 37$  K with a representative value of  $\Omega = 1.366 \times 10^{-3}$  mbar while ignoring background attenuation and Mach discs. There is a clear minimum in the value of the attenuation coefficient at  $\gamma = 0.35$  rad ( $\approx 20^\circ$ ). By comparison to the most popular, and widely available, commercial skimmers available from Beam Dynamics inc. [42], we see that their stock skimmers (model numbers 1 and 2 [43]) have opening half-angles of  $\gamma = 12.5^\circ$  which would result in an approximately 5% larger backscattering attenuation coefficient than our suggested optimal value according to Figure 8 if all other dimensions are the same as modelled here.

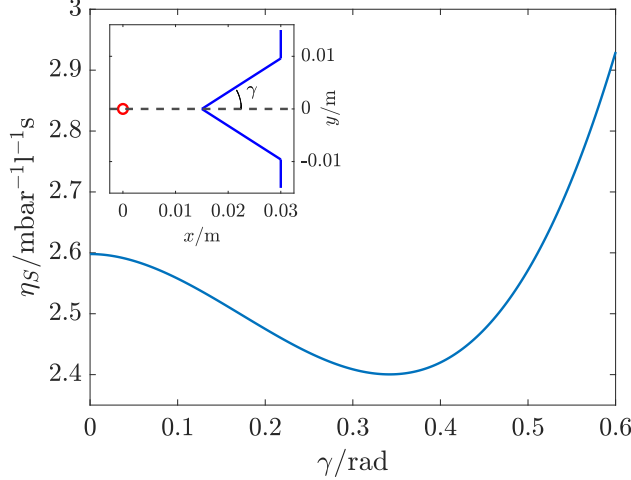


FIG. 8: A plot of the backscattering attenuation coefficient,  $\eta_S$ , as a function of  $\gamma$  for a skimmer (length 15 mm) and back plate (radius 25 mm). As the skimmer broadens, the total interference due to backscattering drops because the skimmer shields an increasing fraction of the mounting plate. The attenuation subsequently reaches a minimum value and rises.

### E. Optimisation of skimmer design

Here we calculate the optimum value for the radius of the circle describing the skimmer arc, given a set of constraints. We stress that current skimmers are perfectly useable and the calculations here serve as a demonstration of the theory. In this example, we take the beam length, skimmer length and skimmer width to be  $d_B = 15$  mm,  $l = 15$  mm and  $w = 10$  mm, respectively. We then vary the radius of curvature  $R_C$ ; a sharper skimmer corresponds to a smaller value of  $R_C$ . Naturally, when designing a real source, all four parameters can be varied and thus must be considered alongside other constraints.

The results are plotted in Figure 9. We consider a  $^4\text{He}$  source at  $T_0 = 37$  K, take  $\Omega = 1.366 \times 10^{-3}$  and neglect background attenuation. Two cases and the optimal design are shown in the inset. Crucially, the results show that a sharper skimmer is not necessarily superior to one with a flatter profile. By minimising  $\eta_S$  with respect to the angle between the skimmer's centre line and wall we can show that the optimal radius of curvature for the skimmer is 41 mm.

## V. CONCLUSIONS

We have described a method for calculating the effect of source chamber interference on the intensity of a free-jet beam. Well-pumped Fenn-type sources were considered, although the results should be applicable to some

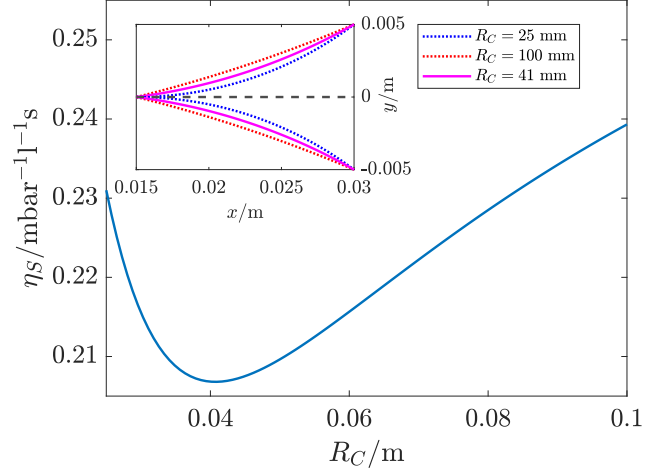


FIG. 9: A plot of the backscattering attenuation coefficient,  $\eta_S$ , for a curved skimmer with a profile described by an arc section with a radius  $R_C$ . The arc is constrained to pass through the beam axis. The width of the skimmer base is fixed at  $w = 10$  mm, its length is  $l = 15$  mm and the beam length is  $d_B = 15$  mm. A broad minimum is observed, showing that the theory can be applied to optimise skimmer designs.

Campargue sources in which the chamber pressure does not completely suppress free molecular flow. Our approach is more straightforward and complete than previous attempts at the problem, as we have shown that the beam attenuation can be described by a single parameter,  $\eta$ , given by an integral expression containing no adjustable parameters. The signal,  $W$ , is proportional to  $Qe^{-\eta Q}$  for nozzle throughput,  $Q$ .  $\eta$  is the sum of two components, due to backscattering and the interaction with the background gas, respectively. Equations (13) and (22), for  $\eta_S$  and  $\eta_B$ , summarise the content of the work and are simple to evaluate numerically. We have also presented three sets of experimental data in Section III to support the results, with good agreement in all cases, particularly with respect to the scaling relationships ( $\eta_S \propto 1/T_0^{11/6}$  and  $\eta_B \propto 1/T_0^{2/3}$ ) predicted by the theory.

We have shown that ‘skimmer interference’ is only significant in typical source-skimmer geometries at low temperatures, whereas the interaction with the background gas leads to attenuation in room-temperature beams. In the sources considered in Subsections IIIB and IIIC, which feature pumping speeds  $S \geq 2500$  L s $^{-1}$  and nozzle-skimmer distances  $\sim 10$  mm, skimmer effects are visible near 150 K but only dominate below  $\sim 50$  K. We have also investigated interference in a series of hypothetical source chambers, assuming low nozzle temperatures, to develop a set of design recommendations. To summarise, we find that (i) surfaces perpendicular to the beam are surprisingly problematic, (ii) narrow skimmers

are not necessarily superior to broader ones and (iii) the theory can be used to optimise skimmer designs.

The benefits of the theory are twofold. First, source chamber interference can now be accounted for straightforwardly when estimating centreline intensities. Even if one suspects that there will be negligible attenuation, it is now easy to check, via the condition  $\eta Q \ll 1$ . Second, the theory allows for the optimisation of skimmers and source chambers. Estimates can now be made of the interference due to alternative designs, and they may be rejected before more effort is devoted to developing them. We anticipate that improvements to existing skimmers can be proposed by combining our theory with further experimental work on both internal/external shock waves.

## VI. ACKNOWLEDGEMENTS

The work was supported by EPSRC grant EP/R008272/1, Innovate UK/Ionoptika Ltd. through Knowledge Transfer Partnership 10000925. The work was carried out in part at CORDE, the Collaborative R&D Environment established to provide access to physics-related facilities at the Cavendish Laboratory, University of Cambridge, and the EPSRC award EP / T00634X / 1. SML acknowledges support from EPSRC grant EP/X525686/1. The authors appreciate the helpful comments and feedback from Boyao Liu, Paul Dastoor and William Allison.

### Appendix A: Complete Derivation of Cross Section

Here we derive the cross section describing the interaction between a beam atom and an interfering particle. Much of the derivation here builds on earlier work by Hedgeland et al. [25], although the final result in the present case is more general.

Consider a particle of the beam travelling along the  $z$ -axis with speed  $v$ . Let the speed of a residual gas molecule be  $u$  and the velocity's direction angle to the negative  $z$ -direction be  $\theta$ . The situation is illustrated in the first panel of Figure 2. The centre of mass (CoM) frame is also depicted there, alongside the instantaneous rest frame (IRF) of the beam atom. In the latter, the speed of the residual atom is  $w = \sqrt{u^2 + v^2 + 2uv \cos \theta}$  and the angle  $\delta$  is given by  $\tan \delta = u \sin \theta / (v + u \cos \theta)$ .

The critical impact parameter for interference with the beam is determined by small-angle scattering. As a result, in the limiting case that defines the cross section, the atoms will barely be deflected from their initial straight-line paths due to their mutual interaction. Let the separation of the two atoms at an instant be  $r = 2r_c$  and the minimum value (i.e. the distance of closest approach) be  $d$ . The trajectory  $r_c = r_c(\psi)$  can therefore be approximated by

$$\frac{d}{2} = r_c \sin \psi, \quad (\text{A1})$$

in the CoM frame. Using that lowest-order solution, it is possible to calculate the perpendicular impulse  $I_\perp = \int F_\perp dt = \int F \sin \psi dt$ , assuming that a van der Waals (VDW) potential,

$$V(r) = -\frac{C_6}{r^6}, \quad (\text{A2})$$

is a suitable model. The central force is given by  $F = -dV/dr$ .  $I_\perp$  is the only non-zero component of the impulse, by symmetry. Both experimental [13] and theoretical [44] values of the coefficient  $C_6$  exist; the DFT value of  $C_6 = 1.46$  a.u. is used in all computations in the main text. Here, 1 a.u. (atomic unit) is equal to  $E_h/a_0^6 = \hbar^2/m_e a_0^8$  for Hartree energy  $E_h$ , electronic mass  $m_e$  and Bohr radius  $a_0$ .

The final expression needed to evaluate the integral for  $I_\perp$  comes from conservation of the angular momentum,  $L$ , of one particle about the CoM,  $O$ ,

$$L = \frac{mwd}{4} = mr_c^2 \dot{\psi}, \quad (\text{A3})$$

so  $\dot{\psi} = wd/4r_c^2$  and  $dt = d\psi/\dot{\psi} = 4r_c^2 d\psi/wd$ .  $m$  is the mass of a gas atom. Hence, the impulse is

$$I_\perp = \frac{3C_6}{16wd} \int_0^\pi \frac{\sin \psi}{r_c^5} d\psi = \frac{15\pi C_6}{8wd^6}. \quad (\text{A4})$$

Now consider an atom travelling towards the beam particle in its IRF at the angle  $\delta$ . The impulse is invariant under the Galilean transformation that relates the second and third frames of Figure 2, so (A4) applies without modification. Let the angle  $\varphi$  parameterise the path of a particular atom, as illustrated by Figure A1, so that the components of the impulse acting on the beam atom are

$$\mathbf{I} = I_\perp \begin{pmatrix} \cos \varphi \\ \sin \varphi \cos \delta \\ \sin \varphi \sin \delta \end{pmatrix}, \quad (\text{A5})$$

with the  $x$ -axis into the page and  $z$ . Only the first two components result in a deflection of the beam atom away from the axis, so the magnitude of the relevant impulse is

$$I = I_\perp \sqrt{\cos^2 \varphi + \sin^2 \varphi \cos^2 \delta}. \quad (\text{A6})$$

Let  $\Omega$  be the angle subtended by the radius of the limiting aperture from the nozzle. For an atom to be deflected such that it fails to reach the detector, its trajectory must be perturbed at least  $\Omega$ . In the limiting case,  $I = mv\Omega$ ,

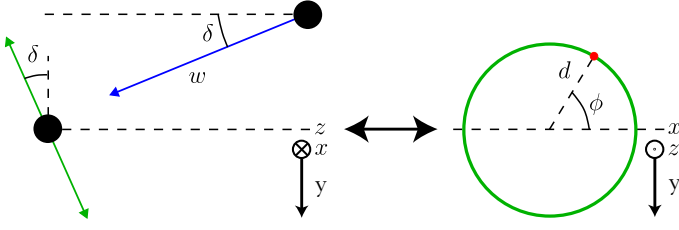


Fig. A1: A sketch showing the circle of possible impulses for a given impact parameter,  $d$ , and hence beam-perpendicular impulse  $I_{\perp}$ . The trajectory of backscattered or background gas atom, indicated by a red dot on the edge of the circle, is parameterised by the angle  $\varphi$ , which is measured with respect to the  $x$ -axis. The total impulse, integrated over the entire trajectory, is perpendicular to the path of the interfering atom.

using the small angle approximation. Let  $d_0$  be the corresponding critical impact parameter. Inserting expressions and rearranging for  $d_0$ ,

$$d_0 = \left( \frac{15\pi C_6}{8mvw\Omega} \right)^{1/6} (\cos^2 \varphi + \sin^2 \varphi \cos^2 \delta)^{1/12}. \quad (\text{A7})$$

$\Omega$  is unlikely to be the angle of the skimmer aperture viewed from the nozzle, which is typically large compared to e.g. a pre-detector aperture. Furthermore, given that  $d < d_0$  leads to deflection,  $d_0$  defines a cross section,  $\sigma = (1/2) \int_{-\pi}^{\pi} d_0^2 d\varphi$ . Using (A7),

$$\sigma = \left( \frac{15\pi C_6}{8mvw\Omega} \right)^{1/3} \int_{-\pi/2}^{\pi/2} (\cos^2 \varphi + \sin^2 \varphi \cos^2 \delta)^{1/6} d\varphi. \quad (\text{A8})$$

The integral in (A8) cannot be evaluated analytically. The result is a generalisation of that in Hegeland et al. [25] to larger angles  $\delta$ ; both expressions are identical to second-order.  $\sigma$  is much larger than a typical hard-sphere cross section because weak interactions are sufficient to cause deflections that prevent transmission to the detector in long-beam axis systems.

### Appendix B: Extension of backscattering formulae to a continuous profile function

Equation (13) for the backscattering attenuation coefficient can be modified for a continuous profile function,  $f(x)$ , where  $x$  is the horizontal distance of a point from the tip of the skimmer. The integral over  $r$  is thus replaced by one over  $x$ .

An infinitesimal element of the profile has length  $dx$  and height  $df$ . Its angle to the  $x$ -axis is therefore given by

$$\tan \gamma = f'(x). \quad (\text{B1})$$

The effective nozzle-tip distance for that element is

$$d_E = x + d - f(x)/f'(x), \quad (\text{B2})$$

The distance of a point  $P$  from the effective tip, at the distance  $d_E$ , is

$$r = f(x) \sqrt{1 + [f'(x)]^{-2}}. \quad (\text{B3})$$

The total length of the element is

$$dr = \sqrt{1 + [f'(x)]^2} dx. \quad (\text{B4})$$

In Appendix C we use this result to evaluate the performance of a parabolic skimmer profile as a function of the outer radius of the skimmer mounting plate,  $r_+$ , and the curvature parameter of a parabolic given by  $f(x) = \epsilon x^2$ .

### Appendix C: Beam attenuation due to backscattered particles - exact and approximate solutions

Here we compare the numerical solution to the exact integral for  $\eta_S$ , (13), with its approximate analytic form (14). In Figure C1 we evaluate (i) the exact numerical solution to (13), (ii) the approximate result with  $\lambda = 0.15$ , and (iii) the approximate result with  $\lambda = 0$ , all as a function of the half angle at the skimmer tip,  $\gamma$ .

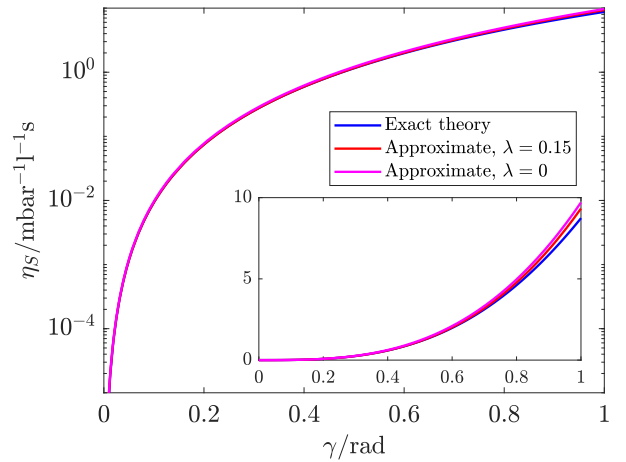


Fig. C1: A plot of the backscattering attenuation coefficient,  $\eta_S$ , as a function of the half angle,  $\gamma$ , defining a conical skimmer. The ramped length and nozzle-skimmer distance are  $a = d_B = 15$  mm. Both the exact and approximate expressions for  $\eta_S$  have been evaluated and plotted, corresponding to Equations (13) and (14), respectively. The same graph with a linear scale is included in the inset.

From Figure C1 there is excellent agreement between the exact and approximate solutions for beam attenuation due to backscattered particles even as  $\gamma \rightarrow 1$ . A significant finding from (14) is that  $\eta_S \propto \gamma^3$ .

Finding an expression for  $\eta_S$  with the inclusion of a skimmer mounting plate (i.e. an element with  $\gamma = \pi/2$ ) is more difficult than doing so for a conical skimmer because a wide range of scattering angles contribute to the attenuation when the element is perpendicular to the beam. Therefore, for a general plate, it is most straightforward to numerically integrate (13). However, an approximate analytic result can be found for the special case of a skimmer mounting plate, positioned such that the skimmer limits the range of scattering angles. The geometry is illustrated by Figure C2.

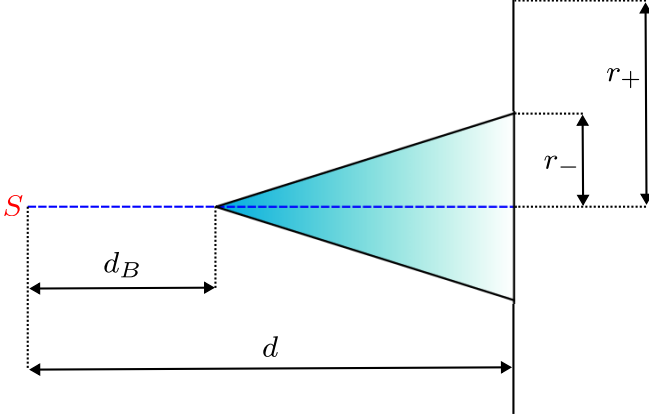


Fig. C2: A skimmer mounting plate. The skimmer, in blue, obscures the part of the beam nearest the plate, so although the nozzle-plate distance is  $d$ , one must integrate from  $z = d - d_B$  to  $d$  when calculating  $\eta_S$ . For  $r_+ \ll d - d_B$ , it is straightforward to find an approximate expression for  $\eta_S$ .

Consider a small plate, extending from  $r = r_-$  to  $r_+$  with  $r_-, r_+ \ll d_B$ . Let  $d$  be the distance between the nozzle and the plate, for consistency with Figure 3. Assuming that all angles (except  $\gamma = \pi/2$ ) are small leads to

$$\eta_S \approx \frac{p+1}{4k_B T_0} \left( \frac{15\pi C_6}{mv_0^4 \Omega} \right)^{1/3} \frac{d_B (r_+^2 - r_-^2)}{d^3 (d - d_B)} I_u. \quad (\text{C1})$$

To further simplify the above,  $\lambda = 0$  can be inserted. In Figure C3, we plot (i) the exact result, (ii) the approximate result with  $\lambda = 0.15$  and (iii) the approximate result with  $\lambda = 0$ . We use  $d_B = 15$  mm,  $d = 30$  mm and  $r_- = 0$ . The contribution from the skimmer is neglected.

To determine  $\eta_S$  due to a narrow parabolic skimmer, we follow the approach outlined in Appendix B, i.e. we describe the profile in terms of the horizontal distance,  $x$ , from the tip. The skimmer may then be described by a profile function  $f(x) = \epsilon x^2$  as long as  $\max(f(x)) \ll d_B$ . Evaluating,

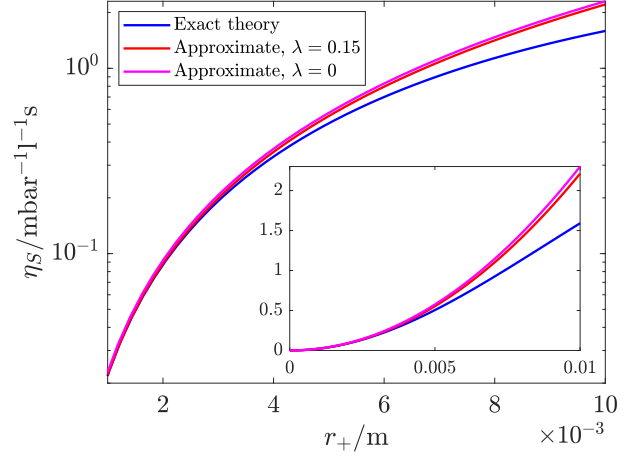


Fig. C3: A plot of the backscattering attenuation coefficient,  $\eta_S$ , as a function of outer radius,  $r_+$ , for a skimmer mounting plate. Figure C2 defines the important quantities; we take  $d = d_B$  and  $r_- = 0$ . Both the exact and approximate expressions have been evaluated and plotted, corresponding to Equations (13) and (C1), respectively. The same graph with a linear scale is included in the inset.

$$\eta_S \approx \frac{(p+1) d_B \epsilon^3}{2k_B T_0} \left( \frac{15\pi C_6}{mv_0^4 \Omega} \right)^{1/3} I_u \times \left\{ \left( \frac{d_B}{x + d_B} \right)^2 \left[ x + \frac{d_B^3}{8(x + d_B)^2} \right] - \frac{3}{2} d_B \ln(x + d_B) + x \right\} \Bigg|_{x_1}^{x_2}, \quad (\text{C2})$$

where  $x_1$  and  $x_2$  define the extent of the skimmer. By altering the limits, one can approximate different curves (e.g. circular arcs) by parabolas to calculate their attenuation coefficients. In Figure C4, we plot (i) the exact result from Equation (13), (ii) the approximate result with  $\lambda = 0.15$  and (iii) the approximate result with  $\lambda = 0$ . We take  $x_1 = 0$  and  $x_2 = d_B = 15$  mm.

#### Appendix D: Beam attenuation due to background particles - exact and approximate solutions

Here we compare the numerical solution to the exact integral for the beam attenuation due to background particles,  $\eta_B$ , as defined exactly in (22), and its approximate analytic form (23). In the following calculations we neglect the Mach disc, take the beam length as  $d_B = 15$  mm, and use a  $^4\text{He}$  beam operating at 37 K with a representative value for  $\Omega = 1.366 \times 10^{-3}$  rad.

The attenuation coefficient due to the diffuse background,  $\eta_B$ , is independent of the geometry of the source,



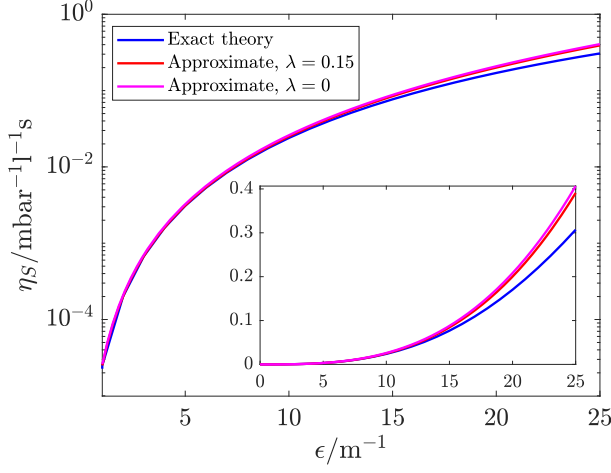


Fig. C4: A plot of the backscattering attenuation coefficient,  $\eta_S$ , as a function of the curvature parameter,  $\epsilon$ , describing a parabolic skimmer with a profile given by  $f(x) = \epsilon x^2$ . The length of the beam and skimmer are  $d_B = x_2 = 15$  mm, and we take  $x_1 = 0$ . Both the exact and approximate expressions have been evaluated, corresponding to Equations (13) and (C2). The same graph with a linear scale is plotted in the inset.

making it difficult to approximate in general. However, for nozzle temperatures  $T_0 \ll T_C$ , an analytic expression can be derived by noting that most of the interfering molecules have speeds,  $u$ , much larger than the beam velocity,  $v_0$ . As a result, the relative speed,  $w$ , satisfies  $w \approx u$  in most scattering events, and

$$\eta_B \approx \frac{5\Gamma(5/6)d_B}{12S} \left[ \frac{30C_6}{\sqrt{\pi}\Omega(mk_B T_C)^2 v_0^4} \right]^{1/3} I_\theta, \quad (\text{D1})$$

where  $\Gamma$  is the gamma function.

$$I_\theta = \int_0^\pi \int_{-\pi/2}^{\pi/2} (\cos^2 \varphi + \sin^2 \varphi \cos^2 \theta)^{1/6} \sin \theta d\varphi d\theta \approx 5.72, \quad (\text{D2})$$

is a numerical constant. We plot the exact and approximate expressions for  $\eta_B$  in Figure D1, using  $T_C = 293$  K and  $S = 2500$   $\text{ls}^{-1}$ . However, a different pumping speed simply leads to a rescaling of all values of the coefficient, because  $\eta_B \propto 1/S$ .

Figure D1 shows excellent agreement for cryogenic nozzle temperatures, but the fractional error rises as nozzle temperatures, and therefore beam, temperature approaches ambient conditions,  $T_0 \rightarrow T_C$ , where  $T_C = 293$  K is the chamber temperature.

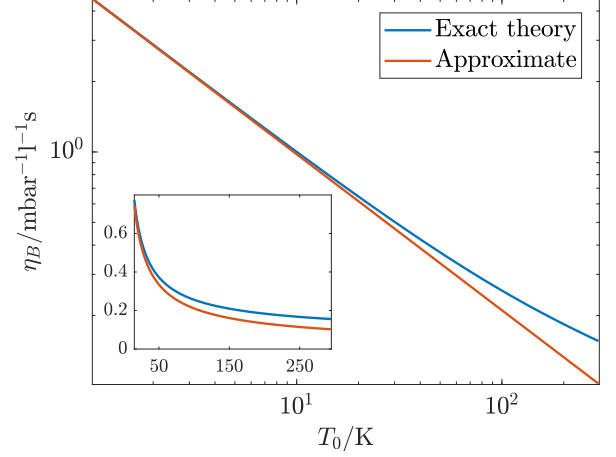


Fig. D1: A plot of the attenuation coefficient due to background gas in the chamber,  $\eta_B$ , as a function of nozzle temperature,  $T_0$ , for  $S = 2500$   $\text{ls}^{-1}$ . Both the exact and approximate results have been evaluated and plotted, corresponding to Equations (22) and (23).

## Appendix E: Skimmer Geometries

Figure E1 shows cross sectional schematic diagrams of the skimmer geometries used in the experimental validation of the presented theory, for which data is contained in Figure 5. Sources 1 and 2 use the simple conical design shown in Panel (a), and Source 3 uses the more complex geometry in Panel (b).

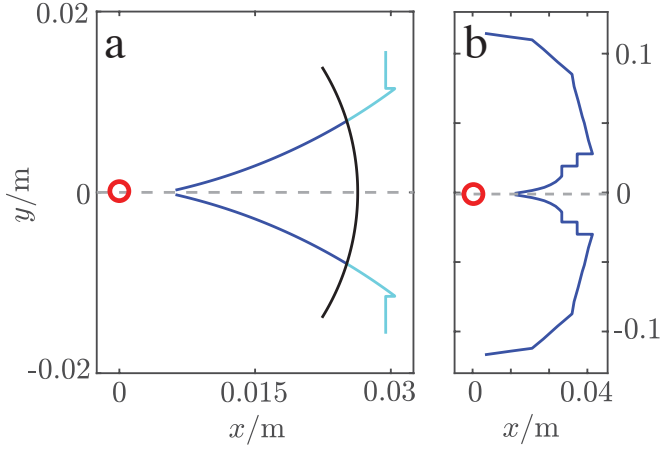


Fig. E1: Schematic cross sections of the two skimmer geometries used to experimentally investigate beam attenuation, relating to data presented in Figure 3. The source nozzle is marked by a red circle, the beam axis is the horizontal dashed line, the Mach disc colour is black, and the skimmer itself is blue/cyan. The varying skimmer colour represents regions which lie within (blue) and outside the Mach disc (cyan). Sources 1 and 2 use the geometry shown in Panel (a), while Source 3 uses the more complex geometry in Panel (b). The Mach disc position in Panel (a) was calculated using  $T_0 = 21$  K.



- [1] S. Kirkpatrick, M. Walsh, R. Svrluga, and J. Khoury, Accelerated neutral atom beam (ANAB) technology for nanoscale surface processing, in *2016 IEEE 16th International Conference on Nanotechnology (IEEE-NANO)* (2016) p. 710.
- [2] C. S. Allred, J. Reeves, C. Corder, and H. Metcalf, Atom lithography with metastable helium, *Journal of Applied Physics* **107**, 10.1063/1.3295903 (2010).
- [3] N. A. von Jeinsen, S. M. Lambrick, M. Bergin, A. Radić, B. Liu, D. Seremet, A. P. Jardine, and D. J. Ward, 2D Helium Atom Diffraction from a Microscopic Spot, *Physical Review Letters* **131**, 236202 (2023), publisher: American Physical Society.
- [4] A. Radić, N. von Jeinsen, K. Wang, Y. Zhu, I. Sami, V. Perez, D. Ward, A. Jardine, M. Chhowalla, and S. Lambrick, Defect density quantification in monolayer MoS<sub>2</sub> using helium atom micro-diffraction, *arXiv* (2024).
- [5] N. von Jeinsen, A. Radić, K. Wang, C. Zhao, V. Perez, Y. Zhu, M. Chhowalla, A. Jardine, D. Ward, and S. Lambrick, Helium atom micro-diffraction as a characterisation tool for 2D materials, *arXiv* (2024).
- [6] A. S. Palau, S. D. Eder, G. Bracco, and B. Holst, Neutral helium atom microscopy, *Ultramicroscopy* **251**, 113753 (2023).
- [7] A. Radić, S. M. Lambrick, N. A. von Jeinsen, A. P. Jardine, and D. J. Ward, 3D surface profilometry using neutral helium atoms, *Applied Physics Letters* **124**, 204101 (2024).
- [8] S. M. Lambrick, M. Bergin, D. J. Ward, M. Barr, A. Fahy, T. Myles, A. Radić, P. C. Dastoor, J. Ellis, and A. P. Jardine, Observation of diffuse scattering in scanning helium microscopy, *Phys. Chem. Chem. Phys.* **24**, 26539 (2022).
- [9] J. Jankunas and A. Osterwalder, Cold and controlled molecular beams: Production and applications, *Annu. Rev. Phys. Chem.* **66**, 241 (2015), <https://doi.org/10.1146/annurev-physchem-040214-121307>.
- [10] P. Kraus, A. Tamtögl, M. Mayrhofer-Reinhartshuber, F. Apolloner, C. Göswiner, S. Miret-Artés, and W. Ernst, Surface structure of Bi(111) from helium atom scattering measurements - inelastic close-coupling formalism, *J. Phys. Chem. C* **119**, 17235 (2015), <https://doi.org/10.1021/acs.jpcc.5b05010>.
- [11] B. Liu, W. Allison, B. Peng, N. Avidor, B. Monserrat, and A. P. Jardine, Distinguishing Quasiparticle-Phonon Interactions by Ultrahigh-Resolution Lifetime Measurements, *Physical Review Letters* **132**, 176202 (2024), publisher: American Physical Society.
- [12] B. Liu, J. Kelsall, D. J. Ward, and A. P. Jardine, Experimental Characterization of Defect-Induced Phonon Lifetime Shortening, *Physical Review Letters* **132**, 056202 (2024), publisher: American Physical Society.
- [13] G. Scoles, *Atomic and molecular beam methods / Vol.1*. (Oxford University Press, 1988).
- [14] M. D. Morse, 2 - supersonic beam sources, *Experimental Methods in The Physical Sciences* **29**, 21 (1996).
- [15] I. Khalil and D. R. Miller, The structure of supercritical fluid free-jet expansions, *AIChE Journal* **50**, 2697–2704 (2004).
- [16] M. Jugroot, C. P. T. Groth, B. A. Thomson, V. Baranov, and B. A. Collings, Numerical investigation of interface region flows in mass spectrometers: neutral gas transport, *Journal of Physics D: Applied Physics* **37**, 1289–1300 (2004).
- [17] G. A. Bird, Transition regime behavior of supersonic beam skimmers, *Phys. Fluids* **19**, 1486 (1976), <https://aip.scitation.org/doi/pdf/10.1063/1.861351>.
- [18] S. D. Eder, A. S. Palau, T. Kaltenbacher, G. Bracco, and B. Holst, Velocity distributions in microskimmer supersonic expansion helium beams: High precision measurements and modeling, *Rev. of Sci. Instrum.* **89**, 113301 (2018), <https://doi.org/10.1063/1.5044203>.
- [19] A. S. Palau, S. D. Eder, T. Andersen, A. K. Ravn, G. Bracco, and B. Holst, Center-line intensity of a supersonic helium beam, *Phys. Rev. A* **98**, 063611 (2018).
- [20] M. Yamashita and J. B. Fenn, Electrospray ion source. another variation on the free-jet theme, *The Journal of Physical Chemistry* **88**, 4451–4459 (1984).
- [21] J. B. Fenn, Mass spectrometric implications of high-pressure ion sources, *International Journal of Mass Spectrometry* **200**, 459–478 (2000).
- [22] R. Campargue, Progress in overexpanded supersonic jets and skimmed molecular beams in free-jet zones of silence, *J. Phys. Chem.* **88**, 4466 (1984), <https://doi.org/10.1021/j150664a004>.
- [23] H. C. W. Beijerinck, R. J. F. van Gerwen, E. R. T. Kerstel, J. F. M. Martens, E. J. W. van Vliembergen, M. r. Th. Smits, and G. H. Kaashoek, Campargue-type supersonic beam sources: Absolute intensities, skimmer transmission and scaling laws for mono-atomic gases he, ne and ar, *Chem. Phys.* **96**, 153 (1985).
- [24] Y. Segev, N. Bibelnik, N. Akerman, Y. Shagam, A. Luski, M. Karpov, J. Narevicius, and E. Narevicius, Molecular beam brightening by shock-wave suppression, *Sci. Adv.* **3**, 1602258 (2017), <https://www.science.org/doi/pdf/10.1126/sciadv.1602258>.
- [25] H. Hedgeland, A. P. Jardine, W. Allison, and J. Ellis, Anomalous attenuation at low temperatures in high-intensity helium beam sources, *Rev. Sci. Instr.* **76**, 123111 (2005).
- [26] M. J. Verheijen, H. C. W. Beijerinck, W. A. Renes, and N. F. Verster, A quantitative description of skimmer interaction in supersonic secondary beams: Calibration of absolute intensities, *Chem. Phys.* **85**, 63 (1984).
- [27] J. Mukherjee, L. M. Gantayet, and S. A. Ahmad, Free jet expansion of atomic beam: simulation studies of some parameters, *J. Phys. D: Appl. Phys.* **33**, 1386 (2000).
- [28] S. Montero, Molecular description of steady supersonic free jets, *Phys. Fluids* **29**, 096101 (2017), <https://doi.org/10.1063/1.5001250>.
- [29] H. C. W. Beijerinck and N. F. Verster, Absolute intensities and perpendicular temperatures of supersonic beams of polyatomic gases, *Physica B+C* **111**, 327 (1981).
- [30] S. M. Lambrick, M. Bergin, A. P. Jardine, and D. J. Ward, A ray tracing method for predicting contrast in neutral atom beam imaging, *Micron* **113**, 61 (2018).
- [31] A. Fahy, S. D. Eder, M. Barr, J. Martens, T. A. Myles, and P. C. Dastoor, Image formation in the scanning helium microscope, *Ultramicroscopy* **192**, 7 (2018).
- [32] S. M. Lambrick, M. Bergin, D. J. Ward, M. Barr, A. Fahy, T. Myles, A. Radić, P. C. Dastoor, J. Ellis, and A. P. Jardine, Observation of diffuse scattering in scanning helium

- microscopy, *Phys. Chem. Chem. Phys.* **24**, 26539 (2022).
- [33] I. Yasumoto, Accommodation coefficients of helium, neon, argon, hydrogen, and deuterium on graphitized carbon, *J. Phys. Chem* **91**, 4298 (1987), <https://doi.org/10.1021/j100300a019>.
- [34] S. C. Saxena and R. K. Joshi, *Thermal Accommodation and Adsorption Coefficients of Gases* (McGraw-Hill, 1982).
- [35] W. S. Young, Derivation of the free-jet mach-disk location using the entropy-balance principle, *Phys. Fluids* **18**, 1421 (1975), <https://aip.scitation.org/doi/pdf/10.1063/1.861039>.
- [36] B. A. J. Lechner, *Studying complex surface dynamical systems using helium-3 spin-echo spectroscopy*, Ph.D. thesis, University of Cambridge (2012).
- [37] A. Jardine, *Quasi-elastic Helium Atom Scattering: Interpretation and Instrumentation*, Ph.D. thesis, University of Cambridge (2001).
- [38] B. A. J. Lechner, H. Hedgeland, W. Allison, J. Ellis, and A. P. Jardine, Note: A new design for a low-temperature high-intensity helium beam source, *Rev. Sci. Instrum.* **84**, 026105 (2013), <https://doi.org/10.1063/1.4791929>.
- [39] D. Chisnall, *A High Sensitivity Detector for Helium Atom Scattering*, Ph.D. thesis, University of Cambridge (2012).
- [40] A. Radic, S. Lambrick, S. Rhodes, and D. J. Ward, On the application of components manufactured with stereolithographic 3d printing in high vacuum systems, *Vacuum* 10.21203/rs.3.rs-3681351/v1 (2023), under Review.
- [41] A. S. Palau, S. D. Eder, T. Andersen, A. K. Ravn, G. Bracco, and B. Holst, Center-line intensity of a supersonic helium beam, *Phys. Rev. A* **98**, 063611 (2018).
- [42] B. D. inc., Beam dynamics home page (2024).
- [43] B. D. inc., Skimmer dimensions (2024).
- [44] T. Gould and T. Bučko, C6 coefficients and dipole polarizabilities for all atoms and many ions in rows 1–6 of the periodic table, *J. Chem. Theory. Comput.* **12**, 3603 (2016), <https://doi.org/10.1021/acs.jctc.6b00361>.